

A transiting, temperate mini-Neptune orbiting the M dwarf TOI-1759 unveiled by *TESS*

NÉSTOR ESPINOZA,¹ ENRIC PALLÉ,² JONAS KEMMER,³ RAFAEL LUQUE,⁴ JOSÉ A. CABALLERO,⁵ CARLOS CIFUENTES,⁵
ENRIQUE HERRERO,^{6,7} VÍCTOR J. SÁNCHEZ BÉJAR,^{2,8} STEPHAN STOCK,³ KARAN MOLAVERDIKHANI,^{3,9,10,11}
GIUSEPPE MORELLO,^{2,8} DIANA KOSSAKOWSKI,⁹ MARTIN SCHLECKER,⁹ PEDRO J. AMADO,⁴ PAZ BLUHM,³
MIRIAM CORTÉS-CONTRERAS,⁵ THOMAS HENNING,⁹ LAURA KREIDBERG,⁹ MARTIN KÜRSTER,⁹ MARINA LAFARGA,^{6,7}
NICOLAS LODIEU,^{2,8} JUAN CARLOS MORALES,^{6,7} MAHMOUDREZA OSHAGH,^{2,8} VERA M. PASSEGGER,^{12,13} ALEXEY PAVLOV,⁹
ANDREAS QUIRRENBACH,³ SABINE REFFERT,³ ANSGAR REINERS,¹⁴ IGNASI RIBAS,^{6,7} ELOY RODRÍGUEZ,⁴
CRISTINA RODRÍGUEZ LÓPEZ,⁴ ANDREAS SCHWEITZER,¹³ TRIFON TRIFONOV,⁹ PRIYANKA CHATURVEDI,¹⁵
STEFAN DREIZLER,¹⁴ SANDRA V. JEFFERS,¹⁶ ADRIAN KAMINSKI,³ MARÍA JOSÉ LÓPEZ-GONZÁLEZ,⁴ JORGE LILLO-BOX,⁵
DAVID MONTES,¹⁷ GRZEGORZ NOWAK,^{2,8} SANTOS PEDRAZ,¹⁸ SIEGFRIED VANAUERBEKE,^{19,20} MARIA R. ZAPATERO OSORIO,²¹
MATHIAS ZECHMEISTER,¹⁴ KAREN A. COLLINS,²² ERIC GIRARDIN,²³ PERE GUERRA,²⁴ RAMON NAVES,²⁴
IAN J.M. CROSSFIELD,²⁵ ELISABETH C. MATTHEWS,²⁶ STEVE B. HOWELL,²⁷ DAVID R. CIARDI,²⁸ ERICA GONZALES,²⁹
RACHEL A. MATSON,³⁰ CHARLES A. BEICHMAN,²⁸ JOSHUA E. SCHLIEDER,³¹ THOMAS BARCLAY,^{32,31} MICHAEL VEZIE,³³
JESUS NOEL VILLASEÑOR,³³ TANSU DAYLAN,³³ ISMAEL MIREIES,³⁴ DIANA DRAGOMIR,³⁴ JOSEPH D. TWICKEN,^{35,27}
JON JENKINS,²⁷ JOSHUA N. WINN,³⁶ DAVID LATHAM,²² GEORGE RICKER,³³ AND SARA SEAGER³³

¹Space Telescope Science Institute, 3700 San Martin Drive, Baltimore, MD 21218, United States of America

²Instituto de Astrofísica de Canarias (IAC), 38205 La Laguna, Tenerife, Spain

³Landessternwarte, Zentrum für Astronomie der Universität Heidelberg, Königstuhl 12, 69117 Heidelberg, Germany

⁴Instituto de Astrofísica de Andalucía (CSIC), Glorieta de la Astronomía s/n, 18008 Granada, Spain

⁵Centro de Astrobiología (CSIC-INTA), ESAC, Camino bajo del castillo s/n, 28692 Villanueva de la Cañada, Madrid, Spain

⁶Institut de Ciències de l'Espai (ICE, CSIC), Campus UAB, c/ de Can Magrans s/n, 08193 Cerdanyola del Vallès, Barcelona, Spain

⁷Institut d'Estudis Espacials de Catalunya (IEEC), c/ Gran Capità 2-4, 08034 Barcelona, Spain

⁸Departamento de Astrofísica, Universidad de La Laguna, 38206 La Laguna, Tenerife, Spain

⁹Max-Planck-Institut für Astronomie, Königstuhl 17, 69117 Heidelberg, Germany

¹⁰Universitäts-Sternwarte, Ludwig-Maximilians-Universität München, Scheinerstrasse 1, 81679 München, Germany

¹¹ORIGINS: Exzellenzcluster Origins, Boltzmannstraße 2, 85748 Garching, Germany

¹²Homer L. Dodge Department of Physics and Astronomy, University of Oklahoma, 440 West Brooks Street, Norman, OK 73019, United States of America

¹³Hamburger Sternwarte, Gojenbergsweg 112, 21029 Hamburg, Germany

¹⁴Institut für Astrophysik, Georg-August-Universität, Friedrich-Hund-Platz 1, 37077 Göttingen, Germany

¹⁵Thüringer Landessternwarte Tautenburg, Sternwarte 5, 07778 Tautenburg, Germany

¹⁶Max-Planck-Institute für Sonnensystemforschung, Justus-von-Liebig-Weg 3, D-37075 Göttingen, Germany

¹⁷Departamento de Física de la Tierra y Astrofísica & IPARCOS-UCM (Instituto de Física de Partículas y del Cosmos de la UCM), Facultad de Ciencias Físicas, Universidad Complutense de Madrid, 28040 Madrid, Spain

¹⁸Centro Astronómico Hispano-Alemán, Observatorio de Calar Alto, Sierra de los Filabres, 04550 Gérgal, Almería, Spain

¹⁹Vereiniging Voor Sterrenkunde, Brugge, Belgium & Centre for mathematical Plasma-Astrophysics, Department of Mathematics, KU Leuven, Celestijnenlaan 200B, 3001 Heverlee, Belgium

²⁰AstroLAB IRIS, Provinciaal Domein "De Palingbeek", Verbrandemolenstraat 5, 8902 Zillebeke, Ieper, Belgium

²¹Centro de Astrobiología (CSIC-INTA), Carretera de Ajalvir km 4, 28850 Torrejón de Ardoz, Madrid, Spain

²²Center for Astrophysics | Harvard & Smithsonian, 60 Garden Street, Cambridge, MA 02138, United States of America

²³Grand Pra Observatory, Switzerland

²⁴Observatori Astronòmic Albanyà, Camí de Bassesgoda s/n, Albanyà 17733, Girona, Spain

²⁵Department of Physics and Astronomy, University of Kansas, Lawrence, KS 66045, United States of America

²⁶Observatoire de l'Université de Genève, Chemin Pegasi 51, 1290 Versoix, Switzerland

²⁷NASA Ames Research Center, Moffett Field, CA 94035, United States of America

²⁸NASA Exoplanet Science Institute/Caltech-IPAC, MC 314-6, 1200 E California Blvd, Pasadena, CA 91125, United States of America

²⁹Department of Astronomy and Astrophysics, University of California, Santa Cruz, CA 95060, United States of America

³⁰U.S. Naval Observatory, Washington, D.C. 20392, USA

³¹NASA Goddard Space Flight Center, 8800 Greenbelt Rd., Greenbelt, MD 20771, United States of America

³²University of Maryland, Baltimore County, 1000 Hilltop Circle, Baltimore, MD 21250, USA

³³Department of Physics and Kavli Institute for Astrophysics and Space Research, Massachusetts Institute of Technology, Cambridge, MA 02139, United States of America

³⁴Department of Physics and Astronomy, University of New Mexico, 210 Yale Blvd NE, Albuquerque, NM 87106, USA

³⁵SETI Institute, Mountain View, CA 94043, USA

³⁶Department of Astrophysical Sciences, Princeton University, 4 Ivy Lane, Princeton, NJ 08544, United States of America

(Received; Revised; Accepted)

Submitted to AAS

ABSTRACT

We report the discovery and characterization of TOI-1759 b, a temperate (400 K) sub-Neptune-sized exoplanet orbiting the M dwarf TOI-1759 (TIC 408636441). TOI-1759 b was observed by *TESS* to transit on sectors 16, 17 and 24, with only one transit observed per sector, creating an ambiguity on the orbital period of the planet candidate. Ground-based photometric observations, combined with radial-velocity measurements obtained with the CARMENES spectrograph, confirm an actual period of 18.85019 ± 0.00014 d. A joint analysis of all available photometry and radial velocities reveal a radius of $3.17 \pm 0.10 R_{\oplus}$ and a mass of $10.8 \pm 1.5 M_{\oplus}$. Combining this with the stellar properties derived for TOI-1759 ($R_{\star} = 0.597 \pm 0.015 R_{\odot}$; $M_{\star} = 0.606 \pm 0.020 M_{\odot}$; $T_{\text{eff}} = 4065 \pm 51$ K), we compute a transmission spectroscopic metric (TSM) value of over 80 for the planet, making it a good target for transmission spectroscopy studies. TOI-1759 b is among the top five temperate, small exoplanets ($T_{\text{eq}} < 500$ K, $R_p < 4 R_{\oplus}$) with the highest TSM discovered to date. Two additional signals with periods of 80 d and > 200 d seem to be present in our radial velocities. While our data suggest both could arise from stellar activity, the later signal’s source and periodicity are hard to pinpoint given the ~ 200 d baseline of our radial-velocity campaign with CARMENES. Longer baseline radial-velocity campaigns should be performed in order to unveil the true nature of this long period signal.

Keywords: planetary systems – stars: individual: TOI-1759 – planets and satellites: gaseous planets – planets and satellites: detection

1. INTRODUCTION

One of the most exciting astronomical developments in the last decade, triggered by improved instrumentation and survey designs, is the detection and characterization of small ($R_p < 4 R_{\oplus}$) exoplanets. The study of transiting, relatively low-temperature small worlds, in particular, promises to provide key information to understand how different environments (e.g. incident stellar fluxes or initial composition) might impact on their bulk properties, and how those might in turn change their atmospheric and interior structures (Dorn et al. 2017; Neil & Rogers 2020; Ma & Ghosh 2021). In addition, these cooler worlds allow us to make connections with the planets in our own Solar System, all of which have equilibrium temperatures smaller than 500 K (hereon referred to as “temperate” exoplanets). These connections, in turn, have key implications for the search for life outside the Solar System, and have the potential to help us improve and refine the concept of planetary habitability itself (Tasker et al. 2017; Meadows & Barnes 2018; Seager et al. 2021).

Detecting these small, temperate exoplanets is, however, challenging. The relatively longer orbital periods needed to have small irradiation levels makes them difficult to detect from the ground using the transit technique, which is why most of the known temperate worlds were detected by the transit survey with the longest continuous time-baseline: the *Kepler* mission (Borucki et al. 2010). While revolutionary in the search and discovery of small worlds — revealing that they are, in fact, among the most abundant population of exoplanets in our galaxy (at least for close-in exoplanets; Fulton & Petigura 2018; Hsu et al. 2019) — the mission provided few systems amenable for further radial-velocity and/or atmospheric characterization, due to the inherent faintness of the stars it surveyed. This detailed characterization is fundamental to understand the overall make-up of these small, distant worlds, and help us understand and uncover their different sub-populations (see, e.g. Zeng et al. 2019; Gupta & Schlichting 2021; Schlichting & Young 2021; Yu et al. 2021). It is also important to understand fundamental exoplanet demographic questions

such as *why* these small worlds are the most numerous in our galaxy (see, e.g. [Kite et al. 2019](#)).

The Transiting Exoplanet Survey Satellite ([Ricker et al. 2015](#), *TESS*) has been crucial to the search for small transiting exoplanets amenable for detailed characterization. To date, it has already doubled the known sample of small, temperate worlds for which masses have been measured with follow-up observations. And after three years of operation, the mission is just starting to exploit its long-time baselines, allowing the discovery of exoplanets on long orbital periods. In this work, we present the detection and characterization of one such system: TOI-1759 b, an 18.85-day sub-Neptune ($R_p = 3.14 R_\oplus$, $M_p = 10.8 M_\oplus$), orbiting a M dwarf star.

This paper is structured as follows. In § 2 we describe the data that was obtained to understand this new exoplanetary system, which includes photometric, spectroscopic and high-resolution imaging data. In § 3 we present the analysis of these data, including the stellar and planetary properties of the system. We discuss our results in § 4, and summarize our main conclusions from this work in § 5.

2. OBSERVATIONS

2.1. *TESS*

Observations from *TESS* for TOI-1759 (TYC 4266-736-1, TIC408636441) were obtained during its second year of operation in its high-cadence, 2-minute exposure mode on Sectors 16 (September to October, 2019), 17 (October to November, 2019) and 24 (April to May, 2020 — see [Figure 1](#) and [2](#); the data are also presented in [Table 6](#)).

The 2-minute cadence data were processed in the *TESS* Science Processing Operations Center (SPOC; [Jenkins et al. 2016](#)) photometry and transit search pipelines ([Jenkins 2002](#); [Jenkins et al. 2010](#)) at NASA Ames Research Center. The *TESS* data validation reports ([Twicken et al. 2018](#); [Li et al. 2019](#)) on TOI-1759 ([Guerrero et al. 2021](#)) show detections of a transiting exoplanet candidate at a 37.7 day period (although the data were also consistent with a planet at half this period, i.e. 18.85 days) and a transit depth of about 2700 ppm. To perform further analyses on this target, we retrieved the Pre-Data-Conditioning (PDC)-corrected photometry ([Stumpe et al. 2012, 2014](#); [Smith et al. 2012](#)) from all sectors from the Mikulski Archive for Space Telescopes (MAST) archive¹, as this is the highest quality photometry from the three *TESS* sectors mentioned

above. After removing the transits of the planet candidate, we ran the Transit Least Squares (TLS; [Hippke & Heller 2019](#)) algorithm on these photometric time series and found no extra significant signals (i.e., signals with a signal-to-noise ratio > 5) in the data.

2.2. Spectroscopy

2.2.1. *CARMENES*

We monitored TOI-1759 with the *CARMENES*² instrument located at the 3.5 m telescope at the Calar Alto Observatory in Almería, Spain, from July 24, 2020 to January 17, 2021. Our data covered a time span of about 175 d, over which we were able to detect significant radial-velocity signals. The spectra were processed following the standard *CARMENES* data flow ([Caballero et al. 2016](#)) that has been extensively used by previous works (e.g. [Zechmeister et al. 2018](#); [Morales et al. 2019](#); [Trifonov et al. 2020](#)). In our analyses, we only used radial-velocities from the visual (VIS) channel which had mean errors of 2.6 m/s. A total of 57 radial-velocity datapoints were used for our analysis, which are presented in [Table 5](#). The spectra used to derive those have a median signal-to-noise ratio of 95 at 840 nm. Data from our infrared channel was not used as their precision (mean error of 10 m/s) was not enough to put meaningful constraints on the radial-velocity variations observed in the VIS channel.

[Figure 3a](#) shows the radial-velocity as a function of time as observed through the VIS channel, which covers the spectral range 520–960 nm with a spectral resolution of $\mathcal{R} = 94\,600$ ([Quirrenbach et al. 2014, 2018](#)). Our campaign allowed us to clearly detect a signal at about 18.5 d (consistent with half the period of the transiting exoplanet detected in the *TESS* photometry, already discussed in [Section 2.1](#)) on top of an additional long-term trend radial-velocity signal. We discuss the details of our analysis of these signals in [Section 3](#).

2.3. Ground-based photometry

Ground-based photometric follow-up observations were performed as part of the *TESS* Follow-up Program’s (TFOP) Subgroup 1 (SG1). Among the observations, a transit of TOI-1759 b in May 21, 2020, was captured by three independent telescopes/observatories: the OAA telescope in the Observatori Astronòmic Albanyà (Albanyà, Spain; 4 hours of total observing time, per point precision of 1140 ppm at 1-minute cadence; *R*-filter observations), the RCO telescope in the Grand-Pra

¹ <https://archive.stsci.edu/>

² Calar Alto high-Resolution search for M dwarfs with Exoearths with Near-infrared and optical Échelle Spectrographs, <http://carmenes.caha.es>

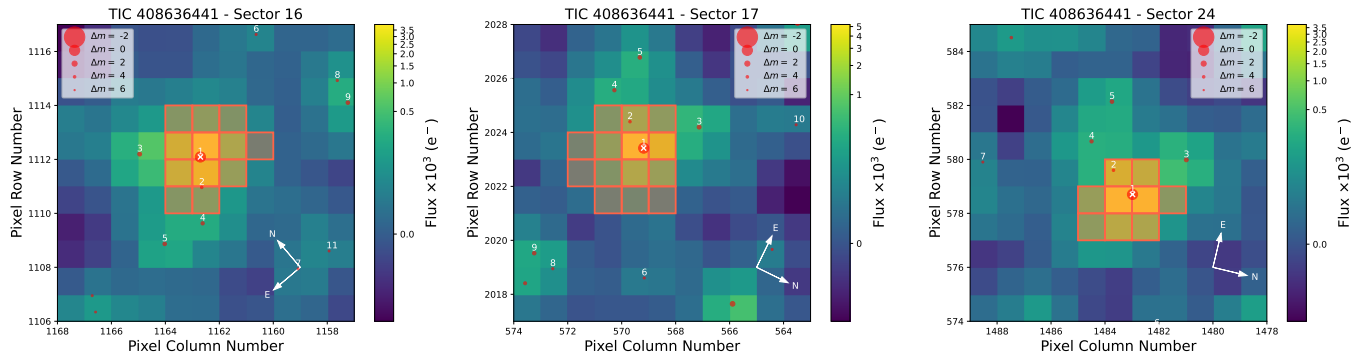


Figure 1. *TESS* target pixel files (TPFs) for TOI-1759 from the different sectors from which data were gathered with the mission (Sector 16 left; 17 center; 24, right). TOI-1759 is marked with a white cross on top of a red point, and is numbered as 1. Smaller numbered red points are the closest stars to the target (drawn from *Gaia*) with *Gaia* magnitude differences with the target of $|\Delta G| < 6$ mag. Contamination is not a problem for TOI-1759, as most nearby targets are very faint. Plot made using *tfplotter* (Aller et al. 2020).

observatory (Valais Sion, Switzerland; 6 hours of total observing time, per point precision of 1080 ppm at 1.3-minute cadence; i_p -filter observations), and the OMC telescope in the Montcabrer observatory (Barcelona, Spain; 5 hours of total observing time, per point precision of 1500 ppm at 1.9-minute cadence; I_c -filter observations). Data reduction for the OAA and OMC observations was performed in a two-step process: the *MaximDL* image processing software was used to perform image calibration (bias, darks, flats), while differential photometry was obtained using the *AstroImageJ* software (Collins et al. 2017). For the RCO observations, image calibration and differential photometry were both performed using *AstroImageJ*. The data, along with a best-fit model transit after subtracting the best-fit systematics model for each dataset (see Section 3 for details), is presented in Figure 4. The data are also presented in Table 6.

The observed transits by these three independent observatories on May 21, 2020 not only confirmed that the event observed by *TESS* was on-target (i.e., happened on TOI-1759), but in practice confirmed that the real period of the event was 18.85 d (i.e., half the period proposed by the *TESS* data validation reports), with the duration and depth detected by those observatories being consistent with the duration and depth observed in the *TESS* transit events.

Long-term photometric monitoring was also performed from the ground using the 0.8 m Joan Oró telescope (TJO; Colomé et al. 2010) at the Montsec Observatory in Lleida, Spain and the 90-cm telescope at the Sierra Nevada Observatory (SNO; Amado et al. 2021). For the TJO observations, the data were obtained from June 2020 to April 2021, spanning for more than 300 d and covering 107 different nights. We obtained a total of 1331 images with an exposure time

of 40 seconds using the Johnson R filter of the LAIA imager, a $4k \times 4k$ CCD with a field of view of $30'$ and a scale of $0.4''/\text{pixel}$. The SNO data were obtained from April to August, 2021, spanning 135 d and collecting observations on 55 different nights. Each night, 20 exposures per filter were obtained using both Johnson V and R filters, with exposure times of 60 and 40 seconds, respectively. The photometry from these exposures was averaged to obtain a single photometric value per filter each night. These data were obtained with a VersArray $2k \times 2k$ CCD camera with a field of view of 13.2×13.2 arcmin² and a scale of 0.4 arcsec/pixel as well.

The TJO CCD images were calibrated with darks, bias and flat fields with the ICAT pipeline (Colomé & Ribas 2006). The differential photometry was extracted with *AstroImageJ* (Collins et al. 2017) using the aperture size that minimized the rms of the resulting relative fluxes, and a selection of the 30 brightest comparison stars in the field which did not show variability. Then, we used our own pipelines to remove outliers and measurements affected by poor observing conditions or presenting a low signal-to-noise ratio. This resulted in a total of 1087 measurements in the final data set with an rms of 6 ppt (parts per thousand).

In a similar way, the SNO resulting light curves were obtained by the method of synthetic aperture photometry. Each CCD frame was also corrected in a standard way for bias and flat-fielding. Different aperture sizes were tested in order to choose the best one for our observations. A number of nearby and relatively bright stars within the frames were selected as reference stars to produce differential photometry of TOI-1759. Finally, outliers due to poor observing conditions or very high airmass were removed. This resulted in a total of 1029 and 1027 individual data points in filters V and R , respectively, with rms of 6.1 and 6.4 ppt.

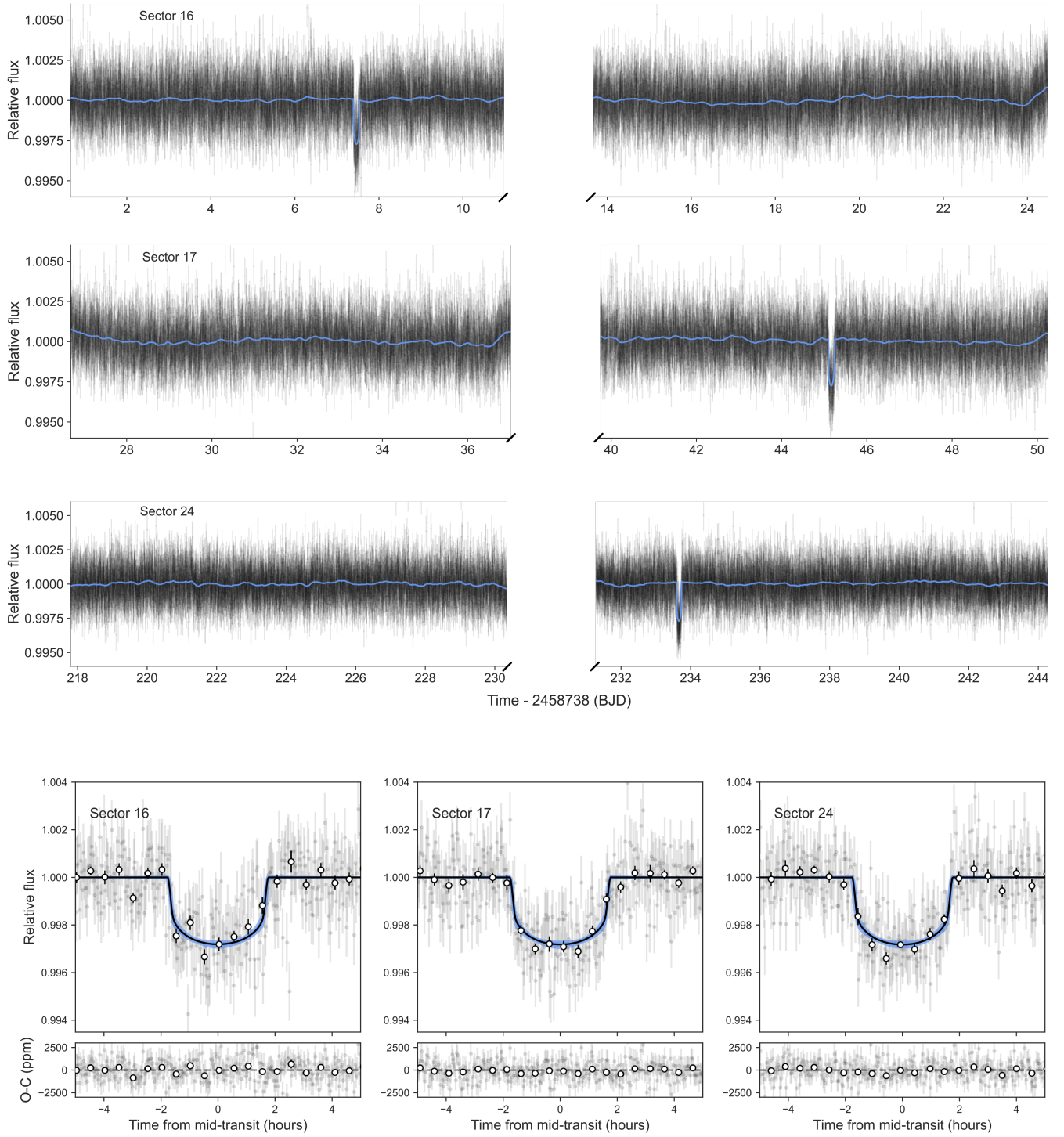


Figure 2. *TESS* transits of TOI-1759 b. The top panels present the *TESS* photometry of TOI-1759 in Sectors 16, 17 and 24 as a function of time (black points with errorbars), along with the best-fit model which consists of a transit model plus a Gaussian process (blue curve). Note there is only a single transit observed in each sector. The bottom panels shows a close-up to each of those transits, which have been phased around the time-of-mid transit (grey points with errorbars); the Gaussian process component has been removed from this photometry. The black line in these panels show the best-fit transit model; blue bands represent the 68% and 95% credibility bands of the model.

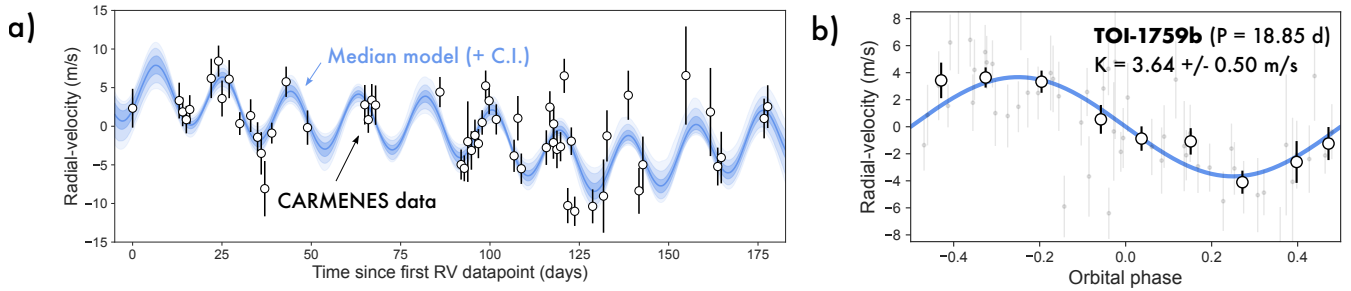


Figure 3. CARMENES radial-velocity follow-up of TOI-1759. **a)** Our CARMENES radial-velocity campaign (white points with black errorbars; first point corresponding to 2459054.56851) had a total duration of about 6 months, over which we were able to detect both a radial-velocity variation at 18.85 d, along with a long-term signal here modeled as a GP. The blue line with transparent bands around it indicate our full (GP + planetary) median signal, along with its 68, 95 and 99% credibility intervals, respectively. **b)** Phase-folded radial-velocity curve at the period of the transiting exoplanet TOI-1759 b ($P = 18.85$ d; grey points, binned datapoints covering about 2 d plotted as white points with black errorbars). The semi-amplitude we obtain for this signal is $3.64 \pm 0.50 \text{ m s}^{-1}$.

Both the TJO and SNO datasets are presented in Table 7. An analysis of these datasets is presented in Section 3.2.

2.4. High-resolution imaging

To help rule out stellar multiplicity and close blends with nearby stars and to obtain more precise planetary radii by accounting for close-in stellar blends (Ciardi et al. 2015; Schlieder et al. 2021), we observed TOI-1759 with both the 'Alopeke³ speckle imaging camera (Scott & Howell 2018) on the 8 m Gemini North telescope and the NIRC2 near-infrared adaptive-optics fed camera on the 10 m Keck-II telescope. The optical and NIR high resolution imaging complement each other with higher resolution in the optical but deeper sensitivity (especially to low-mass stars) in the infrared.

'Alopeke obtains diffraction-limited imaging in two simultaneously-imaged narrow bands centered at 562 and 832 nm. Due to the relative faintness of the target star at these wavelengths, we obtained five exposures in each channel, with integration times of 60 ms each. We reduced the data using standard techniques using the methods described by Matson et al. (2019). The resulting contrast curves and reconstructed 832 nm image, all shown in Fig. 5. The optical speckle observations show no evidence of an additional stellar companion.

TOI-1759 was also observed with the NIRC2 instrument on Keck-II behind the natural guide star AO system (Wizinowich et al. 2000). The observations were made on 2020 Sep 09 UT in the standard 3-point dither pattern that is used with NIRC2 to avoid the left lower quadrant of the detector which is typically noisier than the other three quadrants. The dither pattern step size was 3'' and was repeated twice, with each dither offset from the previous dither by 0.5''. The camera was in the narrow-angle mode with a full field of view of $\sim 10''$ and a pixel scale of approximately 0.0099'' per pixel. The observations were made in the narrow-band $Br\text{-}\gamma$ filter ($\lambda_o = 2.1686$; $\Delta\lambda = 0.0326\mu\text{m}$) with an integration time of 1 seconds with one coadd per frame for a total of 9 seconds on target.

The AO data were processed and analyzed with a custom set of IDL tools. The science frames were flat-fielded and sky-subtracted. The flat fields were generated from a median average of dark subtracted flats taken on-sky, and the flats were normalized such that the median value of the flats is unity. Sky frames were generated from the median average of the 9 dithered science frames; each science image was then sky-subtracted and flat-fielded. The reduced science frames were com-

bined into a single combined image using a intra-pixel interpolation that conserves flux, shifts the individual dithered frames by the appropriate fractional pixels, and median-coadds the frames. The final resolution of the combined dithers was determined from the full-width half-maximum of the point spread function; 0.049''. The sensitivities of the final combined AO image were determined by injecting simulated sources azimuthally around the primary target every 20° at separations of integer multiples of the central source's FWHM (Furlan et al. 2017). The brightness of each injected source was scaled until standard aperture photometry detected it with 5 σ significance. The resulting brightness of the injected sources relative to the target set the contrast limits at that injection location. The final 5 σ limit at each separation was determined from the average of all of the determined limits at that separation and the uncertainty on the limit was set by the rms dispersion of the azimuthal slices at a given radial distance. The final combined image and sensitivity curve are shown in Fig. 6

Both the optical speckle and the near-infrared adaptive optics observations find no additional stars (down to 0.1'' dimmer than about 4-5 magnitudes than the target in the optical and near-infrared) and so further strengthen the case for TOI-1759 b being a bona fide planet.

3. ANALYSIS

3.1. Stellar parameters

We obtained the photospheric parameters T_{eff} , $\log g$ and [Fe/H] of TOI-1759 following Passegger et al. (2019) by fitting PHOENIX synthetic spectra to the combined (co-added) CARMENES VIS spectrum described in Section 2.2.1, which has a signal-to-noise ratio in the VIS channel of ≈ 200 . We used $v \sin i = 2 \text{ km s}^{-1}$, which was measured by Marfil et al. (2021) as an upper limit. We derived its luminosity following Cifuentes et al. (2020) by using the latest parallactic distance from Gaia EDR3 (Gaia Collaboration et al. 2021), and by integrating Gaia, 2MASS (Skrutskie et al. 2006) and AllWISE (Cutri et al. 2014) photometry covering the full spectral energy distribution with the Virtual Observatory Spectral energy distribution Analyser (Bayo et al. 2008). The stellar radius follows from Stefan-Boltzmann's law and the stellar mass by using the linear mass-radius relation from Schweitzer et al. (2019).

TOI-1759's pseudo equivalent width of the H α line as defined by Schöfer et al. (2019) is $\text{pEW}'(\text{H}\alpha) < -0.3 \text{ \AA}$ (Marfil et al. 2021), classifying it as an H α inactive star. Furthermore, Marfil et al. (2021) assign it to the Galactic thin disc population, which has a maximum age of

³ <https://www.gemini.edu/instrumentation/alopeke-zorro>

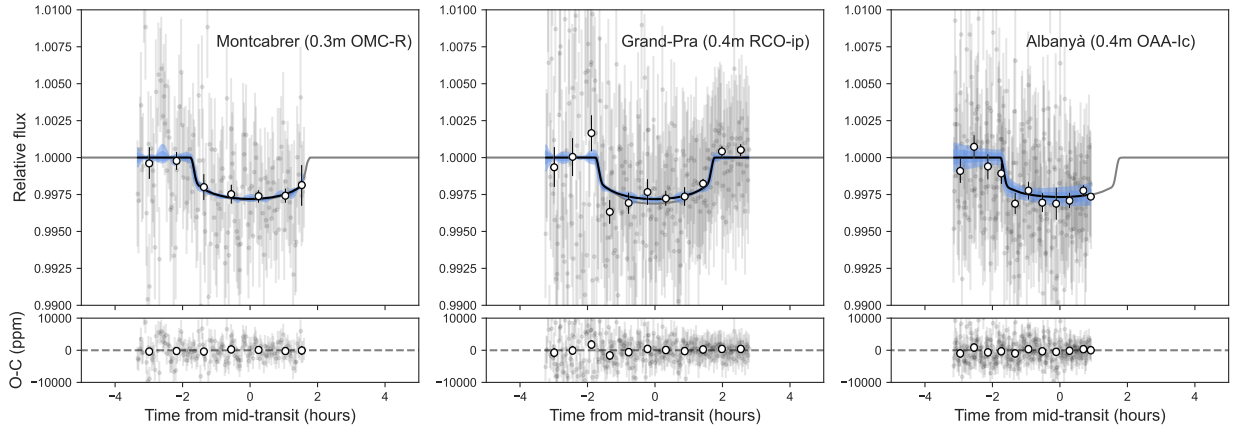


Figure 4. Ground-based follow-up transit photometry of TOI-1759 b. Transit of TOI-1759 b on May 21, 2020, captured by three different observatories: the OAA telescope in the Observatori Astronòmic Albanyà, the RCO telescope in the Grand-Pra Observatory and the OMC telescope in the Motcabrer Observatori. The duration and depth of the event is consistent between instruments.

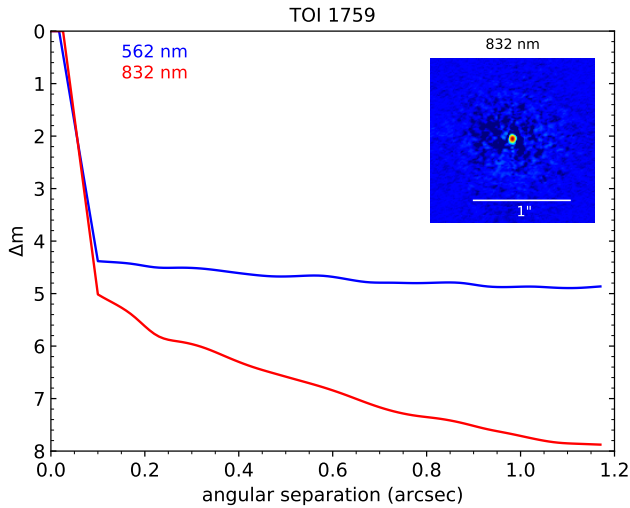


Figure 5. High spatial resolution imaging of TOI-1759. Two-band speckle imaging observations obtained with the Alopeco speckle imaging camera on the 8m Gemini North telescope for TOI-1759 reveal no close-companion down to $0.1''$, dimmer than about $\Delta m = 4-5$ mag than the target.

about 8 Gyr (Fuhrmann 1998). Using these two properties as age indicators, we conclude that its age is between 1 Gyr (the typical minimum age for field stars) and 8 Gyr without being able to be more precise. All collected and derived parameters are presented in Table 1.

3.2. Radial-velocity analysis

We performed a detailed analysis on the radial-velocities described in Section 2.2.1 in order to constrain the possible signals arising from these data. To this end, we performed a suite of model fits to the radial-velocity

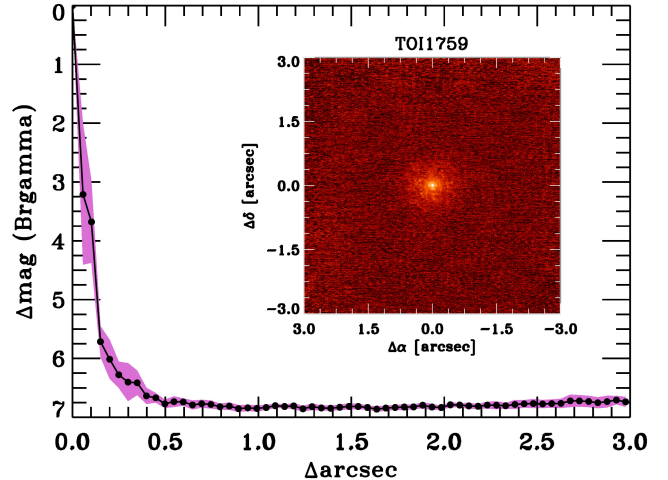


Figure 6. Near-infrared high spatial resolution imaging of TOI-1759. NIRC2 imaging observations obtained for TOI-1759 on Keck-II reveals no close-companion down to $0.1''$, dimmer than about $\Delta m = 4-5$ mag than the target.

data using *juliet* (Espinoza et al. 2019), in order to measure the evidence for a planet in the data using Bayesian evidences, $Z = P(\text{Model}|\text{Data})$. The fits were performed using the Dynamic Nested Sampling algorithm implemented in the *dynesty* library (Speagle 2020).

We considered three main types of radial velocity models. The first was a “no planet” model, namely, a set of models in which it is assumed there is no planetary signal present in the radial-velocity data, and which thus assumes the data are either consistent with a flat line or with correlated noise modeled through a Gaussian process (GP). The second class were “1-planet” models;

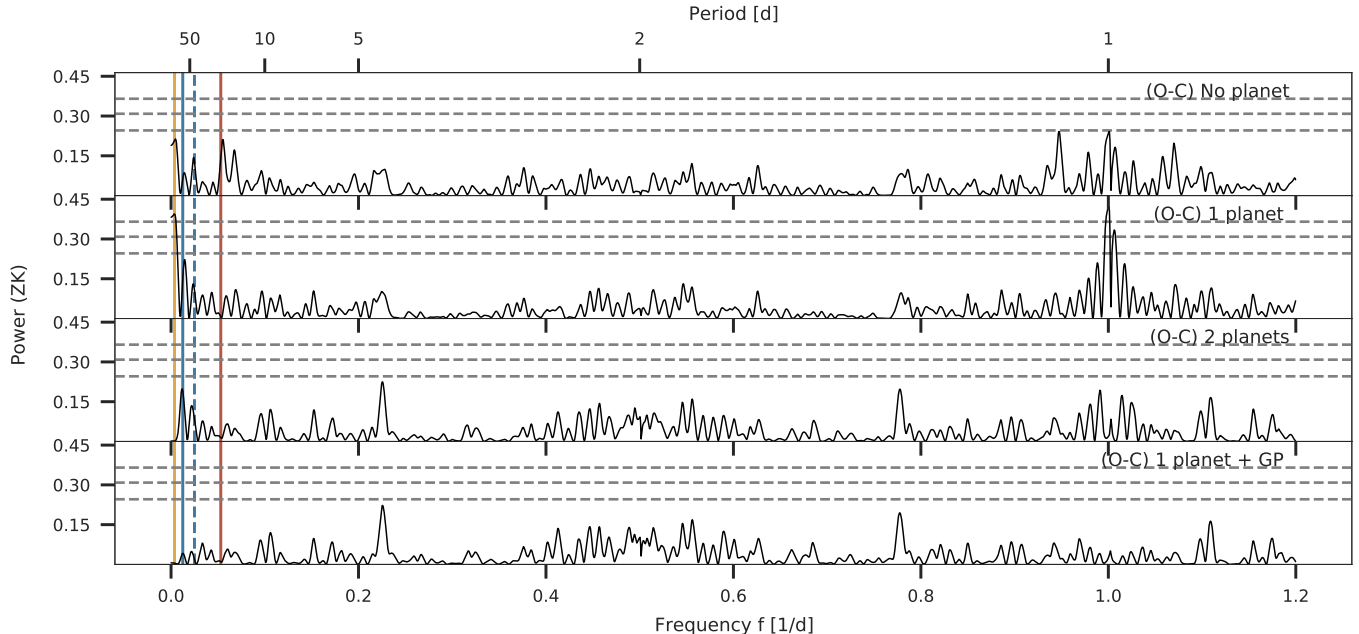


Figure 7. Generalized Lomb-Scargle (GLS) periodograms of the CARMENES radial-velocity data after subtracting different models. The power at each frequency corresponds to the one defined in Zechmeister & Kürster (2009, ZK in the labels above). The period of the transiting planet, $P = 18.85$ d, is marked by the red solid line and the stellar rotation period, $P \approx 80$ d, and its first harmonic with the blue solid and dashed lines respectively. Further, the additional present long term periodicity with $P \approx 270$ d is marked by the yellow solid line. The horizontal dashed grey lines show the analytical false alarm probabilities (FAP) of 10, 1, and 0.1%. The top panel corresponds to the mean-subtracted CARMENES radial-velocity dataset.

these considered the presence of a planetary signal in the radial-velocity data (modeled as a circular orbit), and a suite of possible extra signals, such as linear or quadratic trends, or a (quasi-periodic) GP. Finally, we also considered the possibility that the data was best explained by a “2-planet” model, as a sum of two circular orbits and a suite of possible extra signals, such as a linear, quadratic or a GP trend.

We first performed “blind” fits to the data — that is, fits in which we assumed no strong prior knowledge on the signal(s) present on our radial-velocities. For our GP, we assumed a quasi-periodic kernel of the form

$$k(t_i, t_j) = \sigma_{GP}^2 \exp \left(-\alpha \tau^2 - \Gamma \sin^2 \left[\frac{\pi \tau}{P_{rot}} \right] \right),$$

where $\tau = |t_i - t_j|$. We set log-uniform priors for σ_{GP} , α and Γ , with lower and upper limits of $(0.01, 100) \text{ m s}^{-1}$, $(10^{-10}, 1) \text{ d}^{-1}$ and $(0.01, 100)$ respectively, based on the experiments performed with this kernel in Stock et al. (2020a) and Stock et al. (2020b), and a uniform prior for P_{rot} between 0.5 (half the best sampling in our radial-velocities) and 350 d (two-times our time-baseline). The linear and quadratic trends both had uniform priors on the coefficients of $(10^{-3}, 10^3)$. As for the circular orbits, we set a uniform prior on the period of the first one

from 0.5 to 50 d (so as to cover the 18 and 36-day periods which could possibly originate from the transiting exoplanet), and a uniform prior on the period of the second one from 50 to 350 d. Uniform priors were set for the time of inferior conjunction for both covering the entire time-baseline of our observations, the semi-amplitude — between 0 and 100 m s^{-1} — and the systematic radial velocity — between -100 and 100 m s^{-1} . A jitter term, σ_w was added to all our fits with a log-uniform prior between 0.01 and 100 m s^{-1} .

In our “blind” fits, we found that all models considering a periodic component were consistent with a prominent signal at ~ 18.5 d, which corresponds to the transit signal implied by the *TESS* photometry presented in Section 2.1 and the ground-based transits presented in Section 2.3. The model with the highest evidence in our set of fits was one composed of a sinusoid plus a quasi-periodic GP ($|\Delta \log Z| \approx 4.3$, compared with the no-planets model). Given the high-resolution imaging data presented in Section 2.4, the ground-based transit detected on-target presented in 2.3 and the fact that the period of the planetary signal for the model with the highest evidence ($18.49^{+0.23}_{-0.21}$ d) agrees with the period implied by the photometric data (18.8480 ± 0.0010 d), we consider that this 18-day period signal in both

Table 1. Stellar properties of TOI-1759.

Parameter	Value	Reference
Names	TIC 408636441	TIC
	2MASS J1472477+6245139	2MASS
	TYC 4266-00736-1	Tycho-2
	WISEA J214724.51+624513.8	AllWISE
RA (J2000)	21 ^h 47 ^m 24 ^s .39	<i>Gaia</i> EDR3
DEC (J2000)	62°45′13″.7	<i>Gaia</i> EDR3
Spectral type	M0.0 V	Lep13
$\mu_\alpha \cos \delta$ [mas yr ⁻¹]	-173.425 ± 0.012	<i>Gaia</i> EDR3
μ_δ [mas yr ⁻¹]	-10.654 ± 0.011	<i>Gaia</i> EDR3
π [mas]	24.922 ± 0.010	<i>Gaia</i> EDR3
d [pc]	40.112 ± 0.016	<i>Gaia</i> EDR3
G_{BP} [mag]	11.7164 ± 0.0029	<i>Gaia</i> EDR3
G [mag]	10.8386 ± 0.0028	<i>Gaia</i> EDR3
T [mag]	9.9284 ± 0.0073	TIC
G_{RP} [mag]	9.9174 ± 0.0038	<i>Gaia</i> EDR3
J [mag]	8.771 ± 0.043	2MASS
H [mag]	8.114 ± 0.059	2MASS
K_s [mag]	7.930 ± 0.020	2MASS
$W1$ [mag]	7.825 ± 0.027	AllWISE
$W2$ [mag]	7.886 ± 0.020	AllWISE
$W3$ [mag]	7.787 ± 0.018	AllWISE
$W4$ [mag]	7.643 ± 0.111	AllWISE
L_\star [10 ⁻⁴ L _⊙]	876.7 ± 6.3	This work
T_{eff} [K]	4065 ± 51	This work
log g [dex]	4.65 ± 0.04	This work
[Fe/H] [dex]	0.05 ± 0.16	This work
$v \sin i$ [km s ⁻¹]	≤ 2	Mar21
M_\star [M _⊙]	0.606 ± 0.020	This work
R_\star [R _⊙]	0.597 ± 0.015	This work
Age [Gyr]	1–8	This work
ρ_\star [kg m ⁻³]	3949 ± 323	This work

References—2MASS (Skrutskie et al. 2006), AllWISE (Cutri et al. 2014), *Gaia* EDR3 (Gaia Collaboration et al. 2021), Lep13 (Lépine et al. 2013), Mar21 (Marfil et al. 2021), TIC (Stassun et al. 2019), Tycho-2 (Høg et al. 2000).

photometry and radial-velocities is, indeed, a bona fide transiting exoplanet.

Having concluded that the 18-day period signal is indeed a bona fide transiting exoplanet, we then focused on finding the best model that explains the radial-velocity dataset. We considered the same class of models and priors as the ones presented above, but now for the first planet we fixed the period and transit center to the values defined by a photometric fit made to the data using *juliet* (see Section 3.3 for details on the priors of that fit): period $P = 18.85008 \pm 0.00018$ d, and time-of-transit center $t_0 = 2458745.4651 \pm 0.0015$ d. A compilation of the log-evidences for each of the fits we performed is presented in Table 2. As can be seen, the model with the highest evidence is once again a 1-planet + GP model. Interestingly, however, this model is in practice indistinguishable ($|\Delta \log Z| < 2$; Trotta 2008) from most of the 2-planet models (except the 2-planet + linear trend model). It is also indistinguishable from all those models considering either one or both of them having eccentric orbits.

It is interesting to note that the posterior distribution function of the GP rotation period of the 1-planet + GP model, P_{rot} , shows a bimodal distribution, with peaks at ~ 80 d and > 150 d. In the 2-planet + GP model, the latter long periodic signal is picked up by the second sinusoid and is constrained to be about 270 ± 60 d, while

Table 2. Log-evidence differences ΔZ between different models considered for our radial-velocity-only analysis, assuming one of the Keplerian signals to have the same ephemerides as those implied by the observed transits. Below, a flat-line model includes only a systematic radial-velocity and a jitter term. The GP refers to a Gaussian Process with a quasi-periodic kernel. See text for details on the priors.

Model	$\ln \Delta Z$
<i>No planet models</i>	
Flat line	-9.4
GP	-6.6
<i>1 planet models</i>	
1 planet + linear trend	-23.6
1 planet + quadratic trend	-9.1
1 planet	-8.8
1 planet + GP	0
<i>2 planet models</i>	
2 planet + linear trend	-12.6
2 planet	-1.6
2 planet + GP	-1.4
2 planet + quadratic trend	-1.3

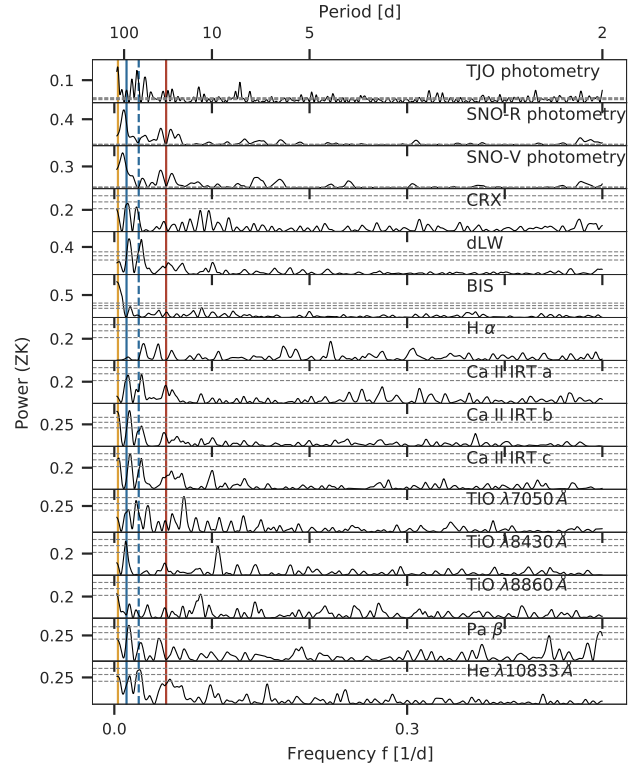


Figure 8. GLS periodograms of the TJO photometry, SNO photometry and the CARMENES spectral activity indicators. Analogous to the periodograms of the RVs, the period of the transiting planet, $P = 18.85$ d and the additional present long term periodicity with $P \approx 270$ d are marked by the solid red and yellow lines, respectively. The stellar rotation period, $P \approx 80$ d, and its first harmonic are indicated by the blue solid and dashed lines. The horizontal dashed grey lines show the analytical false alarm probabilities (FAP) of 10, 1, and 0.1%.

the quasi-periodic component of the GP shows again an accumulation of samples with higher likelihood at ~ 80 d. A Generalized Lomb-Scargle (GLS, Zechmeister & Kürster 2009) periodogram analysis of the residuals of each of those models is presented in Figure 7, in order to further explore the nature of these long-period signals. If the signal of the transiting planet is subtracted (second panel), a significant power excess is apparent at ~ 270 d (which is above the baseline of our observations, which was 175 d) and next to it, even though insignificant, a peak at ~ 80 d. The latter is independent of the long term variation, as it is still present after fitting the transiting planet together with the ~ 270 d signal (third panel).

To find out whether the ~ 80 d signal or the ~ 270 d power excess could be attributed to stellar activity, we investigated the activity indicators that are routinely derived from the CARMENES spectra (see Zechmeis-

ter et al. 2018; Schöfer et al. 2019; Lafarga et al. 2020, for the full list of indicators and how they are calculated). In Figure 8 we show the GLS periodograms of several activity indicators and the long term photometry presented in Section 2.3. Almost all indicators, as well as the photometry, show consistent signals around 80 and/or 40 d, which would explain the ~ 80 d seen in the RVs as the stellar rotation period. If indeed the rotation period of the star is 80 days, the 40-day signal could be interpreted as spots at opposite longitudes and/or a by-product of the not-strictly-periodic nature of the signal. Further, the TJO data, the BIS and the Ca II IRT b and c also show a long term trend, which might be related with the ~ 270 d power excess.

Given that we could not rule out a stellar origin for the ~ 80 d signal and the ~ 270 d power excess, and that the 1-planet + GP model has the highest evidence for our RV data and can account for all significant signals in the data (see the residuals in the last panel of Figure 7), we consider this model for the global modelling of the data which we present in the next subsection. We note that we also tested fitting our global model using the rest of the models in Table 2 which are indistinguishable to the one being selected here, and all of them gave rise to similar constraints in the final parameters of the transiting exoplanet.

3.3. Global modeling

We performed a global modelling of the radial-velocity and photometric data using the `juliet` library (Espinoza et al. 2019) in order to jointly constrain the planetary properties from the photometry and radial-velocity datasets outlined in previous sections. As in the radial-velocity analysis presented in 3.2, we once again use the Dynamic Nested Sampling algorithm implemented in the `dynesty` library (Speagle 2020).

For the *TESS* photometry, we decided to use a GP to consider residual systematic trends in the PDC lightcurves under use in this work. We used an Exponential-Matérn kernel (i.e., the product of an ex-

ponential and a Matérn 3/2 kernel) as implemented in the `celerite` library (Foreman-Mackey et al. 2017) via `juliet`, with hyperparameters (GP amplitude, σ_{GP} , and two time-scales: one for the Matérn 3/2 part of the kernel, ρ , and another for the exponential part of the kernel, T) which are individual to each of the sectors; a jitter term is also added in quadrature to the covariance matrix for each sector. A quadratic law is used to constrain limb-darkening, where the coefficients are shared between the different sectors; we use the parametrization of Kipping (2013) instead of fitting for the limb-darkening coefficients directly. For the ground-based photometry, we found that airmass was a very good predictor of the long-term trends in the data, and so we added this as a linear regressor in our fit — weighted by a coefficient θ , which is different for each instrument and is jointly fit with the rest of the parameters of the global fit. In addition, we observed that this linear regressor was insufficient to model all the correlated noise leftover on the OMC and RCO datasets. We thus decided to fit those with an additional Matérn 3/2 kernel. A linear limb-darkening law was used for all ground-based instruments, as a higher order law was not necessary given the lower photometric precision (see, e.g. Espinoza & Jordán 2016). An individual jitter term was added to the diagonal of the covariance matrix on each of those datasets as well. For the radial-velocities, following our results in Section 3.2, we consider a 1-planet model plus a quasi-periodic GP as the model to be fit in our joint analysis. We set a wide prior for the systemic radial-velocity, as well as for the jitter term and the hyperparameters of the GP — in particular, for the period of the quasi-periodic GP P_{rot} , we use a wide period between 20 and 350 d in order to cover the two possible periods for this parameter observed in Section 3.2. The full definition of the priors and corresponding posteriors of our joint fit are given in Table 3.

Table 3. Prior and posterior parameters of the global fit performed to TOI-1759. For the priors, $N(\mu, \sigma^2)$ stands for a normal distribution with mean μ and variance σ^2 , $TN(\mu, \sigma^2; a, b)$ is a truncated normal distribution with lower and upper limits given by a and b , respectively; $U(a, b)$ and $\log U(a, b)$ stands for a uniform and log-uniform distribution between a and b , respectively.

Parameter	Prior	Posterior
<i>Stellar & planetary parameters</i>		
P_1 [d]	$N(18.85, 0.1^2)$	18.85019 ± 0.00013
$t_{0,1}$ (BJD)	$N(2458745.45, 0.1^2)$	2458745.4654 ± 0.0011
$R_{p,1}/R_\star$	$U(0.0, 1.0)$	0.0483 ± 0.0010
$b_1 = (a/R_\star) \cos(i)$	$U(0.0, 1.0)$	$0.21^{+0.09}_{-0.10}$
K_1 [m s^{-1}]	$U(0, 100)$	$3.64^{+0.50}_{-0.51}$
e_1	fixed	0
ω_1	fixed	90
ρ_\star [kg m^{-3}]	$TN(3949, 323^2; 1000, 10000)$	3970^{+218}_{-233}
<i>TESS photometry instrumental parameters</i>		
$q_{1,TESS}^a$	$U(0, 1)$	$0.32^{+0.24}_{-0.14}$
$q_{2,TESS}^a$	$U(0, 1)$	$0.46^{+0.28}_{-0.25}$
$m_{\text{flux},16}$ [ppm]	$U(0, 10^5)$	851^{+7916}_{-7770}
$m_{\text{flux},17}$ [ppm]	$U(0, 10^5)$	-1598^{+8062}_{-8089}
$m_{\text{flux},24}$ [ppm]	$U(0, 10^5)$	428^{+7904}_{-7797}
$\sigma_{w,16}$ [ppm]	$\log U(0.1, 10^5)$	$1.8^{+7.5}_{-1.5}$
$\sigma_{w,17}$ [ppm]	$\log U(0.1, 10^5)$	$2.9^{+15.1}_{-2.5}$
$\sigma_{w,24}$ [ppm]	$\log U(0.1, 10^5)$	$1.9^{+7.7}_{-1.6}$
$\sigma_{\text{GP},16}$ [ppm]	$\log U(10^{-4}, 10^2)$	$0.000104^{+0.000047}_{-0.000026}$
$\sigma_{\text{GP},17}$ [ppm]	$\log U(10^{-4}, 10^2)$	$0.000106^{+0.000067}_{-0.000040}$
$\sigma_{\text{GP},24}$ [ppm]	$\log U(10^{-4}, 10^2)$	$0.000100^{+0.000030}_{-0.000017}$
$\rho_{\text{GP},16}$ [d]	$\log U(10^{-3}, 10^2)$	73^{+16}_{-17}
$\rho_{\text{GP},17}$ [d]	$\log U(10^{-3}, 10^2)$	74^{+15}_{-18}
$\rho_{\text{GP},24}$ [d]	$\log U(10^{-3}, 10^2)$	76^{+14}_{-17}
$T_{\text{GP},16}$ [d]	$\log U(10^{-3}, 10^2)$	$0.0010^{+0.000047}_{-0.000026}$
$T_{\text{GP},17}$ [d]	$\log U(10^{-3}, 10^2)$	$0.0011^{+0.000081}_{-0.000045}$
$T_{\text{GP},24}$ [d]	$\log U(10^{-3}, 10^2)$	$0.0010^{+0.000034}_{-0.000019}$
<i>Ground-based photometry instrumental parameters</i>		
$q_{1,OAA}$	$U(0, 1)$	$0.41^{+0.27}_{-0.24}$
$q_{1,OMC}$	$U(0, 1)$	$0.55^{+0.27}_{-0.31}$
$q_{1,RCO}$	$U(0, 1)$	$0.50^{+0.30}_{-0.29}$
$m_{\text{flux},OAA}$ [ppm]	$U(0, 10^5)$	-2148^{+214}_{-216}
$m_{\text{flux},OMC}$ [ppm]	$U(0, 10^5)$	7936^{+6471}_{-6203}
$m_{\text{flux},RCO}$ [ppm]	$U(0, 10^5)$	-979^{+6296}_{-5945}
$\sigma_{w,OAA}$ [ppm]	$\log U(0.1, 10^5)$	3395^{+146}_{-140}
$\sigma_{w,OMC}$ [ppm]	$\log U(0.1, 10^5)$	3123^{+202}_{-190}

Table 3 continued

Table 3 (*continued*)

Parameter	Prior	Posterior
$\sigma_{w,\text{RCO}}$ [ppm]	$\log U(0.1, 10^5)$	4143^{+165}_{-158}
θ_{OAA} [d]	$U(-10, 10)$	$0.00112^{+0.00022}_{-0.00021}$
θ_{OMC} [d]	$U(-10, 10)$	$-0.0036^{+0.015}_{-0.015}$
θ_{RCO} [d]	$U(-10, 10)$	$0.013^{+0.015}_{-0.015}$
$\sigma_{\text{GP,OMC}}$ [ppm]	$\log U(10^{-4}, 10^2)$	$0.117^{+0.022}_{-0.012}$
$\rho_{\text{GP,OMC}}$ [d]	$\log U(10^{-3}, 10^2)$	$0.438^{+0.040}_{-0.059}$
$\sigma_{\text{GP,RCO}}$ [ppm]	$\log U(10^{-4}, 10^2)$	$0.117^{+0.019}_{-0.011}$
$\rho_{\text{GP,RCO}}$ [d]	$\log U(10^{-3}, 10^2)$	$0.438^{+0.039}_{-0.051}$
<i>Radial-velocity instrumental/activity parameters</i>		
μ_{CARMENES} [m s^{-1}]	$U(-100, 100)$	$0.1^{+4.7}_{-4.0}$
$\sigma_{w,\text{CARMENES}}$ [m s^{-1}]	$\log U(0.01, 100)$	$1.85^{+0.50}_{-0.49}$
$\sigma_{\text{GP,CARMENES}}$ [m s^{-1}]	$\log U(0.01, 10^2)$	$5.8^{+7.3}_{-2.5}$
$\alpha_{\text{GP,CARMENES}}$ (d^{-1})	$\log U(10^{-10}, 1)$	$0.000011^{+0.000433}_{-0.000011}$
$\Gamma_{\text{GP,CARMENES}}$	$\log U(0.01, 100)$	$0.5^{+2.8}_{-0.5}$
$P_{\text{GP,Rot}}$	$U(20, 350)$	237^{+67}_{-103}

^aThese parameterize the quadratic limb-darkening law using the transformations in [Kipping \(2013\)](#)**Table 4.** Derived properties for TOI-1759 b.

Parameter	Posterior	Description
R_p [R_{\oplus}]	3.14 ± 0.10	Planetary radius
M_p [M_{\oplus}]	10.8 ± 1.5	Planetary mass
i [deg]	89.72 ± 0.13	Orbital inclination
T_{14} [hours]	3.23 ± 0.13	Transit duration
a [au]	0.1177 ± 0.0038	Semi-major axis of the orbit
$T_{eq,0}$ [K]	443 ± 7	Equilibrium temperature ^a (assuming 0 albedo)
$T_{eq,0.3}$ [K]	405 ± 6	Equilibrium temperature ^a (assuming 0.3 albedo)
S_p [S_{\oplus}]	6.39 ± 0.41	Stellar irradiation on the planet
ρ_p [g cm^{-3}]	1.91 ± 0.32	Planetary bulk density
g_p [m s^{-2}]	10.7 ± 1.6	Planetary surface gravity

^aThis assumes perfect energy redistribution.

The resulting best-fit models and corresponding credibility bands are presented in Figure 2 for the *TESS* photometry, in Figure 4 for the ground-based photometry and in Figure 3 for the radial-velocities. The con-

straints from our radial-velocity follow-up allowed us to obtain a precise ($> 5\sigma$ above 0) measurement of the semi-amplitude imprinted by TOI-1759 b on its star of $K = 3.64^{+0.50}_{-0.51} \text{ m s}^{-1}$, which is an over 7-sigma detection of the semi-amplitude. Joining the derived transit and radial-velocity parameters, along with the stellar properties presented in Table 1, we derive the fundamental parameters of TOI-1759 b in Table 4. As can be observed, TOI-1759 b is a relatively cool (443 K equilibrium temperature assuming 0 albedo) sub-Neptune-sized exoplanet ($R_p = 3.14 \pm 0.10 R_{\oplus}$). Coupling these numbers with our estimated mass of $M_p = 10.8 \pm 1.5 M_{\oplus}$, we derive a planetary bulk density ($\rho_p = 1.91 \pm 0.32 \text{ g cm}^{-3}$) and gravity ($g_p = 10.7 \pm 1.6 \text{ m s}^{-2}$) which are strikingly similar to those of Neptune (1.64 g cm^{-3} and 11.15 m s^{-2} , respectively). We discuss the properties of TOI-1759 b in context of other discovered systems in the next section.

4. DISCUSSION

In order to put TOI-1759 b in context with the known sample of small exoplanets, we query the properties of all such exoplanets that (a) have both a measured mass and radius, (b) are smaller than $R_p < 4 R_{\oplus}$ and (c) have equilibrium temperatures cooler than 1000 K from the NASA Exoplanet Archive ([NASA Exoplanet Science Institute 2020](#)) — i.e., a cut similar to that presented in [Guo et al. \(2020\)](#), but updated with the latest exoplan-

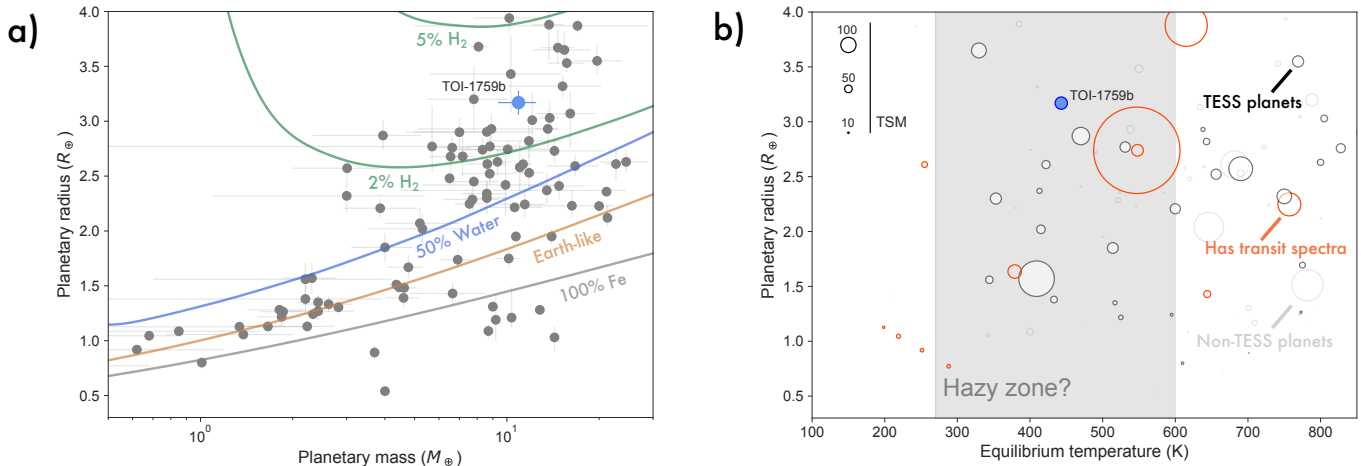


Figure 9. Properties of TOI-1759 b as compared to previously small, known exoplanets with measured mass and radius. **a)** Mass-radius diagram of all known small ($R_p < 4 R_\oplus$) exoplanets with $T_{eq} < 1000$ K (grey) and TOI-1759 b (blue). The mass-radius models are from Zeng et al. (2016) and show 100% Fe (grey), an Earth-like composition (32.5% Fe, 67.5% $MgSiO_3$ by mass, brown), a 50% Earth-like and 50% water-by-mass composition (blue) and Earth-like composition models with 2% and 5% H_2 on top of it (green). Water-rich models with 2% and 5% H_2 on top (i.e., Neptune-like compositions) are not shown, but would be indistinguishable with the green models in this panel given the size of the errorbars. **b)** Equilibrium temperature (assuming zero albedo) versus radius diagram for the same cuts made for panel a), showing the location of *TESS* planets (white markers), non-*TESS* planets (white transparent markers), planets that have previously been characterized via transmission spectroscopy with HST/WFC3 (red markers) and TOI-1759 b (blue). The size of the markers represents the value of the transmission spectroscopy metric (TSM Kempton et al. 2018); grey band shows the proposed region of hazy exoplanets by (Yu et al. 2021, see text for discussion).

etary systems as of July 23, 2021⁴. In Figure 9, we show the location of TOI-1759 b in both the planetary mass versus radius plane and the equilibrium temperature versus planetary radius plane.

In terms of its mass and radius, Figure 9a shows that TOI-1759 b is consistent with having a 2 – 5% H_2 envelope, and an interior composition ranging from being an Earth-like one to being a scaled-down version of Neptune. Figure 9b, on the other hand, shows how TOI-1759 b adds up to the increasing number of small ($R_p < 4 R_\oplus$) worlds with measured mass and radius at relatively low equilibrium temperatures. In particular, TOI-1759 b falls on the very interesting region where the work of Yu et al. (2021) recently proposed exoplanet atmospheres to be hazy due to the lack of haze-removal processes at temperatures between about 300-600 K. It is interesting to note that TOI-1759 b falls *exactly* at the equilibrium temperature where Yu et al. (2021) predict the haziest exoplanets should be ($T_{eq,0.3} \sim 400$ K, where $T_{eq,0.3}$ means an equilibrium temperature calculated assuming an albedo of 0.3; see Table 4). The proposed trend presented in that work seems to be in line with observed transmission spectra

for planets hotter than about 500 K (Crossfield & Kreidberg 2017). For example, GJ 1214 b (550 K, Kreidberg et al. 2014, biggest red circle in Figure 9a) shows a significantly muted water feature, whereas HAT-P-11 b (750 K, Fraine et al. 2014, not shown in Figure 9a as $R_p = 4.3 R_\oplus$ for this exoplanet) has a 3-scale height water amplitude in its transmission spectrum. However, the hypothesis is harder to test for temperate exoplanets (< 500 K), as good targets for atmospheric characterization have remained scarce, in particular for small ($R_p < 4 R_\oplus$) planets.

TOI-1759 b is among the best temperate targets to perform transmission spectroscopy based on its Transmission Spectroscopy Metric (TSM Kempton et al. 2018). Following the work of Kempton et al. (2018), we estimate a TSM of 81 ± 14 , which puts it among the top five targets for atmospheric characterization to date at equilibrium temperatures lower than 500 K, together with L 98-59 d (TSM of 233; Cloutier et al. 2019; Kostov et al. 2019; Pidhorodetska et al. 2021), TOI-178 g (TSM of 114; Leleu et al. 2021), TOI-1231 b (TSM of 97; Burt et al. 2021) and LHS 1140 b (TSM of 89; Dittmann et al. 2017; Ment et al. 2019) — the latter having actually been recently characterized by HST/WFC3 (Edwards et al. 2021), reporting weak evidence for water absorption in its planetary atmosphere.

⁴ More recent queries, along with the same plots shown here, can be generated using the scripts in this repository: <https://github.com/nespinoza/warm-worlds>

For a quantitative assessment of TOI-1759 b’s atmospheric characterization with JWST, we investigated a suite of atmospheric scenarios and calculated their JWST synthetic spectra using the photo-chemical model ChemKM (Molaverdikhani et al. 2019, 2020a), the radiative transfer model petitRADTRANS (Mollière et al. 2019, 2020), and ExoTETHyS (Morello et al. 2021) for uncertainty estimations.

Assuming an isothermal atmosphere with a temperature of 400 K and a constant vertical mixing of $K_{zz}=10^6 \text{ cm}^2 \text{ s}^{-1}$ results in persisting water and methane features in the transmission spectra of TOI-1759 b, see Figure 10. But such atmospheric features are expected to be suppressed in a high-metallicity atmosphere, see bottom panel in Figure 10. Considering haze in the atmosphere of TOI-1759 b further mutes the features and hence a hazy, high-metallicity atmosphere is expected to show a nearly flat transmission spectrum, see the blue line in Figure 10 bottom panel.

The PandExo package (Batalha et al. 2017) was used to determine the best configurations to observe with the NIRISS SOSS (0.6–2.8 μm), NIRSpec G395M (2.88–5.20 μm) and MIRI LRS (5–12 μm) instrumental modes. Then we used ExoTETHyS to compute the simulated spectra. The wavelength bins were specifically determined to have similar counts, leading to nearly uniform error bars per spectral point. Note that the minimal error bars output by ExoTETHyS have been multiplied by the reciprocal of the square root of the observing efficiency and a conservative factor 1.2 that accounts for correlated noise. The resulting error bars are equal to or slightly larger than those obtained with PandExo for the same wavelength bins. In particular, the spectral error bars estimated for just one transit observation per instrument configuration are 25–30 ppm at wavelengths $<5 \mu\text{m}$, and 45–50 ppm at wavelengths $>5 \mu\text{m}$, with several points to sample each molecular feature as shown in Figure 10). Comparing these uncertainties with the expected water and methane features of ~ 200 ppm significance suggests the possibility of differentiating these scenarios during one transit only.

TOI-1759 b, along with TOI-178 g ($R_p = 2.87 R_\oplus$, $T_{eq,0} = 470 \text{ K}$), TOI-1231 b ($R_p = 3.65 R_\oplus$, $T_{eq,0} = 330 \text{ K}$) and the (now) iconic K2-18 b ($R_p = 2.61 R_\oplus$, $T_{eq,0} = 255 \text{ K}$, Benneke et al. 2019; Tsiasaras et al. 2019) form an excellent sample of sub-Neptunes to perform atmospheric characterization via transmission spectroscopy at equilibrium temperatures below 500 K. A sample that can be used to put the prediction of both proposed haze removal (Yu et al. 2021) and methane removal (Molaverdikhani et al. 2020b) processes to the test.

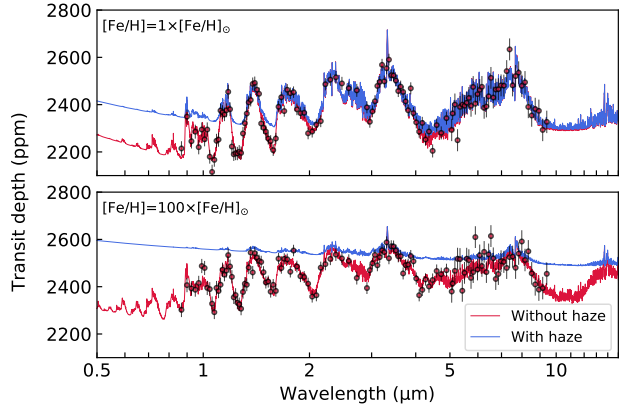


Figure 10. Synthetic JWST transmission atmospheric spectra of TOI-1759 b. Top : Fiducial models with solar abundance, Bottom : Enhanced metallicity by a factor of 100, by considering haze opacity (solid blue lines) and without haze opacity (solid red lines). Estimated uncertainties are shown for the observation of one transit with JWST NIRISS-SOSS, NIRSpec-G395M, and MIRI-LRS configurations.

5. CONCLUSIONS

We have presented the discovery and characterization of the transiting exoplanet TOI-1759 b, a sub-Neptune ($R_p = 3.14 \pm 0.10 R_\oplus$, $M_p = 10.8 \pm 1.5 M_\oplus$) exoplanet on a 18.85-day orbit around an M dwarf star. The initial identification of the target was made thanks to precise *TESS* photometry, which unveiled three transits of the exoplanet in three different sectors with an ambiguous period being consistent with both, a 18.85 and a 37.7-day period exoplanet. Thanks to ground-based photometric follow-up from different observatories, high-resolution spatial imaging and precise radial-velocities from the CARMENES high-resolution spectrograph, we were able to not only confirm TOI-1759 b as a bona fide transiting exoplanet and precisely measure its mass, but also constrain its true period to be $18.85019 \pm 0.00013 \text{ d}$.

TOI-1759 b adds to the growing number of temperate ($T_{eq} < 500 \text{ K}$) exoplanets, and is a particularly promising target to perform atmospheric characterization on. Its equilibrium temperature ($T_{eq,0.3} = 405 \pm 6 \text{ K}$) puts it exactly where the work of Yu et al. (2021) predicts the haziest exoplanets to be, and thus provides an exciting system in which to test this proposal. In addition, our 6-month radial-velocity campaign revealed an 80-day periodicity in the data most likely arising from stellar activity, and a possible longer-term periodicity with a period $> 200 \text{ d}$. The current baseline of our CARMENES observations is insufficient to unveil the true nature of this latter long-period signal. However, a campaign span-

ning a longer baseline is needed in order to reveal the exact source and periodicity of this signal.

CARMENES is an instrument at the Centro Astronómico Hispano-Alemán (CAHA) at Calar Alto (Almería, Spain), operated jointly by the Junta de Andalucía and the Instituto de Astrofísica de Andalucía (CSIC). CARMENES was funded by the Max-Planck-Gesellschaft (MPG), the Consejo Superior de Investigaciones Científicas (CSIC), the Ministerio de Economía y Competitividad (MINECO) and the European Regional Development Fund (ERDF) through projects FICTS-2011-02, ICTS-2017-07-CAHA-4, and CAHA16-CE-3978, and the members of the CARMENES Consortium (Max-Planck-Institut für Astronomie, Instituto de Astrofísica de Andalucía, Landessternwarte Königstuhl, Institut de Ciències de l’Espai, Institut für Astrophysik Göttingen, Universidad Complutense de Madrid, Thüringer Landessternwarte Tautenburg, Instituto de Astrofísica de Canarias, Hamburger Sternwarte, Centro de Astrobiología and Centro Astronómico Hispano-Alemán), with additional contributions by the MINECO, the Deutsche Forschungsgemeinschaft through the Major Research Instrumentation Programme and Research Unit FOR2544 “Blue Planets around Red Stars”, the Klaus Tschira Stiftung, the states of Baden-Württemberg and Niedersachsen, and by the Junta de Andalucía. This work was based on data from the CARMENES data archive at CAB (CSIC-INTA). We acknowledge financial support from the Agencia Estatal de Investigación of the Ministerio de Ciencia, Innovación y Universidades and the ERDF through projects PID2019-109522GB-C5[1:4], PGC2018-098153-B-C33, AYA2018-84089, PID2019-107061GB-C64, PID2019-110689RB-100 AYA2016-79425-C3-1/2/3-P and BES-2017-080769, and the Centre of Excellence “Severo Ochoa” and “María de Maeztu” awards to the Instituto de Astrofísica de Ca-

narias (CEX2019-000920-S), Instituto de Astrofísica de Andalucía (SEV-2017-0709), and Centro de Astrobiología (MDM-2017-0737), NASA (NNX17AG24G), and the Generalitat de Catalunya/CERCA programme. Data were partly collected with the 90-cm telescope at the Sierra Nevada Observatory (SNO) operated by the Instituto de Astrofísica de Andalucía (IAA, CSIC). We acknowledge the telescope operators from the Sierra Nevada Observatory for their support. G. M. has received funding from the European Union’s Horizon 2020 research and innovation programme under the Marie Skłodowska-Curie grant agreement No 895525. This research has made use of the NASA Exoplanet Archive, which is operated by the California Institute of Technology, under contract with the National Aeronautics and Space Administration under the Exoplanet Exploration Program. We acknowledge the use of public TESS data from pipelines at the TESS Science Office and at the TESS Science Processing Operations Center. Resources supporting this work were provided by the NASA High-End Computing (HEC) Program through the NASA Advanced Supercomputing (NAS) Division at Ames Research Center for the production of the SPOC data products. The authors wish to recognize and acknowledge the very significant cultural role and reverence that the summit of Maunakea has always had within the indigenous Hawaiian community. We are most fortunate to have the opportunity to conduct observations from this mountain.

Facilities: TESS, CARMENES/3.5-m Calar Alto telescope, TJO, SNO, AAM, MONTSEC, Keck telescope, Gemini-North telescope.

Software: radvel (Fulton et al. 2018), batman (Kreidberg 2015), juliet (Espinoza et al. 2019), astroimagej (Collins et al. 2017), tpfplotter (Aller et al. 2020), dynesty (Speagle 2020), celerite (Foreman-Mackey et al. 2017).

APPENDIX

A. RADIAL-VELOCITY DATA

Our full CARMENES dataset for the VIS channel is presented in Table 5, along with the corresponding activity indicators at each epoch.

B. PHOTOMETRIC DATA

Our full photometric dataset targeting transits of TOI-1759 is presented in Table 6. The long-term photometry is presented in Table 7.

REFERENCES

- Aller, A., Lillo-Box, J., Jones, D., Miranda, L. F., & Barceló Forteza, S. 2020, A&A, 635, A128
- Amado, P. J., Bauer, F. F., Rodríguez López, C., et al. 2021, A&A, 650, A188

Table 5. Radial velocity measurements for the star along with activity indicators at each epoch.

Name	BJD -2450000	RV (m s ⁻¹)	σ_{RV} (m s ⁻¹)	CRX (m s ⁻¹ Np ⁻¹)	dLW (10 ³ m ² s ⁻²)	BIS (km s ⁻¹)	H α (km s ⁻¹)	Ca II IRT a (km s ⁻¹)	Instrument	S/N
TOI-1759	9054.56851	2.33	2.51	49.44	1.48	-0.0774	0.074	0.0094	CARMENES-VIS	119.4
TOI-1759	9067.60481	3.32	2.32	43.58	-0.04	-0.0646	0.082	0.0128	CARMENES-VIS	97.6
TOI-1759	9068.57556	1.86	1.86	29.70	-11.16	-0.0776	0.074	0.0290	CARMENES-VIS	94.3
TOI-1759	9069.59957	0.86	1.78	21.57	-5.31	-0.0635	0.054	0.0154	CARMENES-VIS	101.8
TOI-1759	9070.55690	2.17	1.85	7.88	-5.34	-0.0764	0.076	0.0237	CARMENES-VIS	111.2
TOI-1759	9076.57116	6.20	2.55	15.86	-22.86	-0.0763	0.078	0.0304	CARMENES-VIS	80.6
TOI-1759	9078.60935	8.44	2.01	18.62	-11.90	-0.0719	0.068	0.0068	CARMENES-VIS	103.2
TOI-1759	9079.59579	3.59	2.33	36.88	-16.68	-0.0677	0.079	0.0154	CARMENES-VIS	104.2
TOI-1759	9081.58773	6.10	2.47	-16.45	-19.67	-0.0604	0.079	0.0099	CARMENES-VIS	81.8
TOI-1759	9084.55634	0.35	1.48	-10.41	2.25	-0.0560	0.093	0.0120	CARMENES-VIS	103.7
TOI-1759	9087.59796	1.37	2.12	6.67	-1.17	-0.0517	0.069	0.0071	CARMENES-VIS	104.8
TOI-1759	9089.53629	-1.43	1.95	-8.83	-5.14	-0.0600	0.071	0.0110	CARMENES-VIS	109.4
TOI-1759	9090.55842	-3.51	2.75	-8.03	-14.72	-0.0490	0.069	0.0033	CARMENES-VIS	76.3
TOI-1759	9091.54399	-8.08	3.58	-32.14	-6.07	-0.0609	0.049	0.0216	CARMENES-VIS	48.5
					...					
TOI-1759	9173.30701	-3.00	2.43	-12.31	12.00	-0.0291	0.052	0.0104	CARMENES-VIS	93.4
TOI-1759	9174.31626	-2.65	1.89	-11.97	15.74	-0.0118	0.065	-0.0023	CARMENES-VIS	90.7
TOI-1759	9175.35015	6.53	2.21	-32.46	7.19	-0.0132	0.102	0.0127	CARMENES-VIS	77.8
TOI-1759	9176.32926	-10.27	2.28	-14.38	20.12	-0.0227	0.064	0.0020	CARMENES-VIS	114.3
TOI-1759	9177.32923	-1.93	1.78	-35.19	13.28	-0.0312	0.066	0.0014	CARMENES-VIS	111.0
TOI-1759	9178.28239	-11.01	1.90	-15.77	7.78	-0.0338	0.086	0.0099	CARMENES-VIS	95.8
TOI-1759	9183.29700	-10.37	2.20	-31.60	-2.18	-0.0157	0.071	0.0123	CARMENES-VIS	97.3
TOI-1759	9186.33693	-9.05	4.74	-45.55	-22.24	-0.0773	0.037	0.0161	CARMENES-VIS	27.1
TOI-1759	9187.30129	-1.25	3.31	-45.82	-24.91	-0.0299	0.103	-0.0038	CARMENES-VIS	50.3
TOI-1759	9193.27483	4.02	3.18	0.08	-0.95	-0.0247	0.084	-0.0052	CARMENES-VIS	64.2
TOI-1759	9196.26135	-8.36	2.97	-9.94	7.30	-0.0186	0.032	-0.0079	CARMENES-VIS	72.1
TOI-1759	9197.34852	-4.98	3.64	-22.89	-3.08	-0.0198	0.085	0.0218	CARMENES-VIS	57.4
TOI-1759	9209.39053	6.56	6.36	7.17	-27.90	-0.0371	0.026	0.0052	CARMENES-VIS	25.7
TOI-1759	9216.25949	1.84	5.71	-48.81	3.21	-0.0156	0.125	0.0121	CARMENES-VIS	38.2
TOI-1759	9218.29595	-5.22	2.45	-15.32	-17.68	-0.0126	0.082	0.0091	CARMENES-VIS	61.6
TOI-1759	9219.28687	-4.05	3.34	-61.08	-22.66	-0.0350	0.055	0.0109	CARMENES-VIS	47.8
TOI-1759	9231.28008	1.00	2.57	-4.70	3.51	-0.0059	0.052	-0.0024	CARMENES-VIS	92.8
TOI-1759	9232.28137	2.54	2.77	-4.43	10.19	-0.0298	0.052	-0.0001	CARMENES-VIS	96.4

NOTE— Signal-to-noise ratio (S/N) for CARMENES-VIS data corresponds to the S/N at order 36 (at about 840 nm). A sample of the full radial-velocity dataset and activity indicators are shown here. The entirety of this table is available in a machine-readable form in the online journal.

Table 6. Photometric transits of the planet.

Name	BJD	Relative flux	Error	Instrument	Standarized airmass
	-2450000				
TOI-1759	8738.65456	1.000458	0.001213	TESS - Sector 16	—
TOI-1759	8738.65594	0.999531	0.001211	TESS - Sector 16	—
TOI-1759	8738.65733	1.000397	0.001213	TESS - Sector 16	—
TOI-1759	8738.65872	1.001858	0.001212	TESS - Sector 16	—
TOI-1759	8738.66011	0.999702	0.001212	TESS - Sector 16	—
TOI-1759	8738.66150	0.999855	0.001212	TESS - Sector 16	—
TOI-1759	8738.66289	0.999816	0.001210	TESS - Sector 16	—
TOI-1759	8738.66428	0.999837	0.001209	TESS - Sector 16	—
TOI-1759	8738.66567	0.998040	0.001210	TESS - Sector 16	—
TOI-1759	8738.66706	0.998851	0.001212	TESS - Sector 16	—
TOI-1759	8738.66844	0.999615	0.001213	TESS - Sector 16	—
	...				
TOI-1759	8990.54955	0.995134	0.001107	Albanya-0.4m (OAA-Ic)	-1.372
TOI-1759	8990.55022	1.000704	0.001110	Albanya-0.4m (OAA-Ic)	-1.380
TOI-1759	8990.55090	0.998573	0.001110	Albanya-0.4m (OAA-Ic)	-1.388
TOI-1759	8990.55159	0.997527	0.001110	Albanya-0.4m (OAA-Ic)	-1.396
TOI-1759	8990.55225	0.999177	0.001110	Albanya-0.4m (OAA-Ic)	-1.403
TOI-1759	8990.55293	1.001281	0.001110	Albanya-0.4m (OAA-Ic)	-1.411
TOI-1759	8990.55360	0.998378	0.001107	Albanya-0.4m (OAA-Ic)	-1.419
TOI-1759	8990.55428	0.998890	0.001113	Albanya-0.4m (OAA-Ic)	-1.426
TOI-1759	8990.55496	0.998735	0.001113	Albanya-0.4m (OAA-Ic)	-1.434
TOI-1759	8990.55563	0.997969	0.001113	Albanya-0.4m (OAA-Ic)	-1.442

NOTE— The Standarized Airmass column corresponds to the airmass values substracted by their mean and divided by their standard deviation. A sample of the full photometric dataset is shown here. The entirety of this table is available in a machine-readable form in the online journal or the source file used to generate this compiled PDF version.

Table 7. Long-term photometric measurements of TOI-1759.

Name	BJD	Relative flux	Error	Instrument
	-2450000			
TOI-1759	9010.61701	0.993732	0.000714	Joan-Oro-0.8m (TJO)
TOI-1759	9010.61758	0.993128	0.000714	Joan-Oro-0.8m (TJO)
TOI-1759	9010.61813	0.991751	0.000714	Joan-Oro-0.8m (TJO)
TOI-1759	9010.61868	0.992962	0.000714	Joan-Oro-0.8m (TJO)
TOI-1759	9010.61923	0.992559	0.000714	Joan-Oro-0.8m (TJO)
TOI-1759	9010.61978	0.990158	0.000714	Joan-Oro-0.8m (TJO)
TOI-1759	9010.62033	0.990918	0.000714	Joan-Oro-0.8m (TJO)
TOI-1759	9010.62089	0.991625	0.000714	Joan-Oro-0.8m (TJO)
TOI-1759	9010.62145	0.992897	0.000719	Joan-Oro-0.8m (TJO)
TOI-1759	9010.62200	0.991557	0.000719	Joan-Oro-0.8m (TJO)
TOI-1759	9010.62255	0.991023	0.000719	Joan-Oro-0.8m (TJO)
		...		
TOI-1759	9457.65199	1.003121	0.001813	Sierra-Nevada-0.9m (SNO-V)
TOI-1759	9457.65339	1.005637	0.001809	Sierra-Nevada-0.9m (SNO-V)
TOI-1759	9457.65479	1.003229	0.001785	Sierra-Nevada-0.9m (SNO-V)
TOI-1759	9457.65619	1.003976	0.001838	Sierra-Nevada-0.9m (SNO-V)
TOI-1759	9457.65759	1.003824	0.001882	Sierra-Nevada-0.9m (SNO-V)
TOI-1759	9457.65899	1.006960	0.001844	Sierra-Nevada-0.9m (SNO-V)
TOI-1759	9457.66039	1.001677	0.001862	Sierra-Nevada-0.9m (SNO-V)
TOI-1759	9457.66320	1.000984	0.001788	Sierra-Nevada-0.9m (SNO-V)
TOI-1759	9457.66460	1.005191	0.001829	Sierra-Nevada-0.9m (SNO-V)
TOI-1759	9457.66600	1.002202	0.001869	Sierra-Nevada-0.9m (SNO-V)

NOTE— A sample of the full photometric dataset is shown here. The entirety of this table is available in a machine-readable form in the online journal or the source file used to generate this compiled PDF version.

- Batalha, N. E., Mandell, A., Pontoppidan, K., et al. 2017, *PASP*, 129, 064501
- Bayo, A., Rodrigo, C., Barrado Y Navascués, D., et al. 2008, *A&A*, 492, 277
- Benneke, B., Wong, I., Piaulet, C., et al. 2019, *ApJL*, 887, L14
- Borucki, W. J., Koch, D., Basri, G., et al. 2010, *Science*, 327, 977
- Burt, J. A., Dragomir, D., Mollière, P., et al. 2021, arXiv e-prints, arXiv:2105.08077
- Caballero, J. A., Guàrdia, J., López del Fresno, M., et al. 2016, in *Society of Photo-Optical Instrumentation Engineers (SPIE) Conference Series*, Vol. 9910, *Observatory Operations: Strategies, Processes, and Systems VI*, ed. A. B. Peck, R. L. Seaman, & C. R. Benn, 99100E
- Ciardi, D. R., Beichman, C. A., Horch, E. P., & Howell, S. B. 2015, *ApJ*, 805, 16
- Cifuentes, C., Caballero, J. A., Cortés-Contreras, M., et al. 2020, *A&A*, 642, A115
- Cloutier, R., Astudillo-Defru, N., Bonfils, X., et al. 2019, *A&A*, 629, A111
- Collins, K. A., Kielkopf, J. F., Stassun, K. G., & Hessman, F. V. 2017, *AJ*, 153, 77
- Colomé, J., Francisco, X., Ribas, I., Casteels, K., & Martín, J. 2010, in *Society of Photo-Optical Instrumentation Engineers (SPIE) Conference Series*, Vol. 7740, *Software and Cyberinfrastructure for Astronomy*, ed. N. M. Radziwill & A. Bridger, 774009
- Colome, J., & Ribas, I. 2006, *IAU Special Session*, 6, 11
- Crossfield, I. J. M., & Kreidberg, L. 2017, *AJ*, 154, 261
- Cutri et al., R. M. 2014, *VizieR Online Data Catalog*, 2328

- Dittmann, J. A., Irwin, J. M., Charbonneau, D., et al. 2017, *Nature*, 544, 333
- Dorn, C., Venturini, J., Khan, A., et al. 2017, *A&A*, 597, A37
- Edwards, B., Changeat, Q., Mori, M., et al. 2021, *AJ*, 161, 44
- Espinoza, N., & Jordán, A. 2016, *MNRAS*, 457, 3573
- Espinoza, N., Kossakowski, D., & Brahm, R. 2019, *MNRAS*, 490, 2262
- Foreman-Mackey, D., Agol, E., Angus, R., & Ambikasaran, S. 2017, *AJ*, 154, 220. <https://arxiv.org/abs/1703.09710>
- Fraine, J., Deming, D., Benneke, B., et al. 2014, *Nature*, 513, 526
- Fuhrmann, K. 1998, *A&A*, 338, 161
- Fulton, B. J., & Petigura, E. A. 2018, *AJ*, 156, 264
- Fulton, B. J., Petigura, E. A., Blunt, S., & Sinukoff, E. 2018, *PASP*, 130, 044504
- Furlan, E., Ciardi, D. R., Everett, M. E., et al. 2017, *AJ*, 153, 71
- Gaia Collaboration, Smart, R. L., Sarro, L. M., et al. 2021, *A&A*, 649, A6
- Guerrero, N. M., Seager, S., Huang, C. X., et al. 2021, *ApJS*, 254, 39
- Guo, X., Crossfield, I. J. M., Dragomir, D., et al. 2020, *AJ*, 159, 239
- Gupta, A., & Schlichting, H. E. 2021, *MNRAS*, 504, 4634
- Hippke, M., & Heller, R. 2019, *A&A*, 623, A39
- Høg, E., Fabricius, C., Makarov, V. V., et al. 2000, *A&A*, 355, L27
- Hsu, D. C., Ford, E. B., Ragozzine, D., & Ashby, K. 2019, *AJ*, 158, 109
- Jenkins, J. M. 2002, *ApJ*, 575, 493
- Jenkins, J. M., Chandrasekaran, H., McCauliff, S. D., et al. 2010, in *Society of Photo-Optical Instrumentation Engineers (SPIE) Conference Series*, Vol. 7740, *Software and Cyberinfrastructure for Astronomy*, ed. N. M. Radziwill & A. Bridger, 77400D
- Jenkins, J. M., Twicken, J. D., McCauliff, S., et al. 2016, in *Proc. SPIE*, Vol. 9913, *Software and Cyberinfrastructure for Astronomy IV*, 99133E
- Kempton, E. M. R., Bean, J. L., Louie, D. R., et al. 2018, *PASP*, 130, 114401
- Kipping, D. M. 2013, *MNRAS*, 435, 2152
- Kite, E. S., Fegley, Bruce, J., Schaefer, L., & Ford, E. B. 2019, *ApJL*, 887, L33
- Kostov, V. B., Schlieder, J. E., Barclay, T., et al. 2019, *AJ*, 158, 32
- Kreidberg, L. 2015, *PASP*, 127, 1161
- Kreidberg, L., Bean, J. L., Désert, J.-M., et al. 2014, *Nature*, 505, 69
- Lafarga, M., Ribas, I., Lovis, C., et al. 2020, *A&A*, 636, A36
- Leleu, A., Alibert, Y., Hara, N. C., et al. 2021, *A&A*, 649, A26
- Lépine, S., Hilton, E. J., Mann, A. W., et al. 2013, *AJ*, 145, 102
- Li, J., Tenenbaum, P., Twicken, J. D., et al. 2019, *PASP*, 131, 024506
- Ma, Q., & Ghosh, S. K. 2021, *MNRAS*, 505, 3853
- Marfil, E., Taberner, H. M., Montes, D., et al. 2021, *arXiv e-prints*, arXiv:2110.07329
- Matson, R. A., Howell, S. B., & Ciardi, D. R. 2019, *AJ*, 157, 211
- Meadows, V. S., & Barnes, R. K. 2018, *Factors Affecting Exoplanet Habitability*, ed. H. J. Deeg & J. A. Belmonte, 57
- Ment, K., Dittmann, J. A., Astudillo-Defru, N., et al. 2019, *AJ*, 157, 32
- Molaverdikhani, K., Helling, C., Lew, B. W., et al. 2020a, *Astronomy & Astrophysics*, 635, A31
- Molaverdikhani, K., Henning, T., & Mollière, P. 2019, *The Astrophysical Journal*, 883, 194
- . 2020b, *The Astrophysical Journal*, 899, 53
- Mollière, P., Wardenier, J., van Boekel, R., et al. 2019, *Astronomy & Astrophysics*, 627, A67
- Mollière, P., Stolker, T., Lacour, S., et al. 2020, *Astronomy & Astrophysics*, 640, A131
- Morales, J. C., Mustill, A. J., Ribas, I., et al. 2019, *Science*, 365, 1441
- Morello, G., Zingales, T., Martin-Lagarde, M., Gastaud, R., & Lagage, P.-O. 2021, *AJ*, 161, 174
- NASA Exoplanet Science Institute. 2020, *Planetary Systems Table*, IPAC, doi:10.26133/NEA12. <https://catcopy.ipac.caltech.edu/doi/doi.php?id=10.26133/NEA12>
- Neil, A. R., & Rogers, L. A. 2020, *ApJ*, 891, 12
- Passegger, V. M., Schweitzer, A., Shulyak, D., et al. 2019, *A&A*, 627, A161
- Pidhorodetska, D., Moran, S. E., Schwieterman, E. W., et al. 2021, *arXiv e-prints*, arXiv:2106.00685
- Quirrenbach, A., Amado, P. J., Caballero, J. A., et al. 2014, in *Proc. SPIE*, Vol. 9147, *Ground-based and Airborne Instrumentation for Astronomy V*, 91471F
- Quirrenbach, A., Amado, P. J., Ribas, I., et al. 2018, in *Society of Photo-Optical Instrumentation Engineers (SPIE) Conference Series*, Vol. 10702, *Ground-based and Airborne Instrumentation for Astronomy VII*, 107020W
- Ricker, G. R., Winn, J. N., Vanderspek, R., et al. 2015, *Journal of Astronomical Telescopes, Instruments, and Systems*, 1, 014003

- Schlichting, H. E., & Young, E. D. 2021, arXiv e-prints, arXiv:2107.10405
- Schlieder, J. E., Gonzales, E. J., Ciardi, D. R., et al. 2021, *Frontiers in Astronomy and Space Sciences*, 8, 63
- Schweitzer, A., Passegger, V. M., Cifuentes, C., et al. 2019, *A&A*, 625, A68
- Schöfer, P., Jeffers, S. V., Reiners, A., et al. 2019, *A&A*, 623, A44
- Scott, N. J., & Howell, S. B. 2018, in *Society of Photo-Optical Instrumentation Engineers (SPIE) Conference Series*, Vol. 10701, *Optical and Infrared Interferometry and Imaging VI*, ed. M. J. Creech-Eakman, P. G. Tuthill, & A. Mérand, 107010G
- Seager, S., Petkowski, J. J., Günther, M. N., et al. 2021, *Universe*, 7, 172
- Skrutskie, M. F., Cutri, R. M., Stiening, R., et al. 2006, *AJ*, 131, 1163
- Smith, J. C., Stumpe, M. C., Van Cleve, J. E., et al. 2012, *PASP*, 124, 1000
- Speagle, J. S. 2020, *MNRAS*, 493, 3132
- Stassun, K. G., Oelkers, R. J., Paegert, M., et al. 2019, *AJ*, 158, 138
- Stock, S., Kemmer, J., Reffert, S., et al. 2020a, *A&A*, 636, A119
- Stock, S., Nagel, E., Kemmer, J., et al. 2020b, *A&A*, 643, A112
- Stumpe, M. C., Smith, J. C., Catanzarite, J. H., et al. 2014, *PASP*, 126, 100
- Stumpe, M. C., Smith, J. C., Van Cleve, J. E., et al. 2012, *PASP*, 124, 985
- Tasker, E., Tan, J., Heng, K., et al. 2017, *Nature Astronomy*, 1, 0042
- Trifonov, T., Lee, M. H., Kürster, M., et al. 2020, *A&A*, 638, A16
- Trotta, R. 2008, *Contemporary Physics*, 49, 71
- Tsiaras, A., Waldmann, I. P., Tinetti, G., Tennyson, J., & Yurchenko, S. N. 2019, *Nature Astronomy*, 3, 1086
- Twicken, J. D., Catanzarite, J. H., Clarke, B. D., et al. 2018, *PASP*, 130, 064502
- Wizinowich, P., Acton, D. S., Shelton, C., et al. 2000, *PASP*, 112, 315
- Yu, X., He, C., Zhang, X., et al. 2021, *Nature Astronomy*, doi:10.1038/s41550-021-01375-3.
<https://doi.org/10.1038/s41550-021-01375-3>
- Zechmeister, M., & Kürster, M. 2009, *A&A*, 496, 577
- Zechmeister, M., Reiners, A., Amado, P. J., et al. 2018, *A&A*, 609, A12
- Zeng, L., Sasselov, D. D., & Jacobsen, S. B. 2016, *ApJ*, 819, 127
- Zeng, L., Jacobsen, S. B., Sasselov, D. D., et al. 2019, *Proceedings of the National Academy of Science*, 116, 9723